Asia-Pacific Journal of Atmospheric Sciences (2024) 60:679–692
https://doi.org/10.1007/s13143-024-00376-2

Online ISSN 1976-7951
Print ISSN 1976-7633

ORIGINAL ARTICLE

Potential Precursory Signals of Localized Torrential Rainfall From Geostationary Satellite and Radar Observations: A Case Study of the 2022 Seoul Flood

Gyuyeon Kim[1] · Yong-Sang Choi[1] · Junho Ho[2]

Received: 11 December 2023 / Revised: 15 June 2024 / Accepted: 30 June 2024 / Published online: 18 July 2024
© The Author(s) 2024

Abstract
The Korean Peninsula frequently experiences localized torrential rainfall (LTR) in the summer. However, on August 8, 2022, a peculiar LTR occurred by the continuous generation of convective clouds within a few hours, numerical weather prediction model was hard to forecast such a high intensity of LTR. This study explores the possibility of uncovering potential precursory signals using remote sensing techniques in both Geostationary Korea Multi-Purpose Satellite 2A (GK2A) and the operational RKSG (Camp Humphreys) Weather Surveillance Radar 88 Doppler (WSR-88D). Using cloud properties from GK2A, cloud top temperature showed a decrease and maintained low values below 220 K 1–1.5 h before the LTR events. However, discerning the exact onset of LTR in already mature stage clouds using only GK2A variables proved challenging. Instead, liquid water content from RKSG sharply increased before the LTR started. Our calculation of the LTR potential from a combination of GK2A and RKSG cloud properties shows a more accurate precursory signal of LTR than from GK2A cloud properties solely or RKSG either. This study highlights the synergistic benefits of combining geostationary satellite and radar observations to understand and predict early precursors of LTR events.

Keywords Localized Torrential Rainfall · Cloud Properties · Convective Clouds · Satellite · Radar

1 Introduction

The Korean Peninsula in East Asia frequently experiences heavy rainfall in the summer. A significant portion of the annual precipitation occurs during the summer season and the frequency of heavy rainfall events has increased (Jung et al. 2011). Recent studies have claimed an increased frequency of localized torrential rainfalls (LTR) consisting 80% of heavy rainfall events from 1992 to 2011 (Jung et al. 2011). LTR events were observed almost annually, with substantial accumulated rainfall, such as September 2005 (Lee and Kim 2007), July 2009 (Jeong et al. 2016), and August 2018 (Shin et al. 2022).

Major efforts to predict LTR events have been conducted primarily based on numerical forecasting models (e.g., Lee and Kim 2007; Jeong et al. 2016; Hong et al. 2018; Shin et al. 2022). Models have been utilized to advance our understanding of the dynamic, thermodynamic, and microphysical processes in clouds that cause heavy rainfall. The Korean Integrated Model (KIM) developed by the Korea Institute of Atmospheric Prediction Systems (KIAPS) is an optimized numerical forecasting model for the Korean meteorological environment (Hong et al. 2018). KIM is used as a useful tool for simulating meteorological environments to predict weather forecasts in Korea (Jeong et al. 2016; Lee and Baik 2016, 2018).

However, LTR events are driven by the rapid development of convective clouds (CC) within hours or less, making it challenging to detect CC with numerical models. Instead, geostationary satellites provide real-time high spatiotemporal resolution data, enabling rapid monitoring of meteorological conditions (Sieglaff et al. 2011; Ivanova 2019; Müller et al. 2022). Cloud properties are derived from atmospheric

Communicated by Hyo-Jong Song.

✉ Yong-Sang Choi
ysc@ewha.ac.kr

[1] Department of Climate and Energy Systems Engineering, Ewha Womans University, EngineerB 353, 52 Ewhayeodae-gil, Seodaemun-gu, Seoul 03760, South Korea

[2] School of Meteorology, University of Oklahoma, Norman, OK, USA

radiation information observed by geostationary satellites, allowing for an understanding of the physical characteristics of CC (Ma et al. 2020). In addition, dual-polarization radars are widely utilized to understand LTR events for its advantages in providing detailed information about the size, shape, composition, phase, orientation, and type of particles within CC (e.g., Doviak and Zrníc Dúsn 1993; You et al. 2019). Polarimetric S-band weather radars are less affected by attenuation and are commonly used to analyze the vertical structure and microphysical properties of LTR events (e.g., Ellis and Vivekanandan 2011; Haberlie and Ashley 2019). Although radar has these advantages, it can only observe after precipitation begins, and has difficulties detecting precursors of CC development. Therefore, previous studies utilized both remote sensing instruments to enhance the accuracy of rainfall estimation and severe weather prediction (Roebeling and Holleman 2009; Okazaki et al. 2019; Jones et al. 2023).

On August 8, 2022, a peculiar LTR occurred in the Seoul metropolitan area of South Korea, with a maximum hourly rainfall of 141.5 mm hr^{-1} measured at a weather station. The convective available potential energy (CAPE) was high enough (> 2,300 m^2/s^2) and convective inhibition (CIN) was very low at 2 m^2/s^2 showing favorable conditions for CC formation (Jung et al. 2015; Park and Park 2020). The Korea Meteorological Administration (KMA) informed heavy rain but did not expect such a high intensity of LTR (Kim et al. 2023b). This is because the formation of CC was expected, but predicting its several occurrences was challenging. This phenomenon is called a back-building type of mesoscale convective system (MCS) and is known for its rarity (e.g., Bluestein and Jain 1985; Chappell 1986; Schumacher and Johnson 2005; Hitchcock and Schumacher 2020). The quasi-stationary characteristics of CCs due to their continuous formation in place can cause heavy rainfall (Schumacher and Johnson 2005; Lee and Kim 2007; Jeong et al. 2016; Ha et al. 2011). The back-building MCS generated as the maintenance of convective updrafts on the storm's upstream flank and the continuous warm and moist supply from the southwesterly low-level jet promotes the formation of new CC (Schumacher and Johnson 2005; Jeong et al. 2016; Schumacher 2017). Although rainfall intensity can be predicted based on the size of the typhoon or the stagnation of the monsoon front (Shin et al. 2022), predicting multiple occurrences of LTR becomes difficult when continuous CC is generated, as observed in this case. Therefore, unprecedented LTR occurred.

The purpose of this study is to explore the possibility of uncovering potential precursory signals of LTR events using a combination of satellite and radar. Since CC develops rapidly within a short time before LTR, we use the two remote sensing measurements with high spatial-temporal resolutions to analyze the cloud properties that can lead to LTR occurrences in the development of CC. This is a preliminary study based on a case, but may serve to improve nowcasting for the future LTRs. Section 2 discusses the characteristics of cloud properties that can detect CC using data from the satellite and radar. In Sect. 3, we analyze the precursory phenomena before LTR events by temporal scene analysis of cloud properties and their changes. Section 4 explores the possibility of quantifying the LTR precursory signals by satellite and radar. Finally, the conclusions and discussions are presented in Sect. 5.

2 Cloud Properties from Satellite and Radar Remote Sensing Data

Geostationary satellites (Sieglaff et al. 2011; Ivanova 2019; Ma et al. 2020; Müller et al. 2022) and radar (You et al. 2019) are valuable measurements to monitor the life cycle of CC that triggers LTR. Therefore, understanding each measurement's characteristics, strengths, and weaknesses is crucial. Geostationary satellites are advantageous for observing rapidly developing clouds due to their ability to monitor fixed areas with high temporal resolution. They offer the advantage of monitoring extensive areas. Since satellites observe cloud tops from space, identifying the composition of particles inside the clouds is difficult. Therefore, as clouds develop vertically, the lower-level cloud particles and precipitation near the ground cannot be observed. On the other hand, radars have limitations in directly observing the early stages of convective initiation but provide more detailed information of inner clouds during precipitation. The microphysical properties and phase (i.e., ice, rain, or mixed-phase precipitation) of hydrometeors can be inferred from polarimetric radar variables to conduct hydrometeor classification, quantitative precipitation estimation, and microphysics retrievals of liquid water content (LWC), volume-weighted mean diameter (D_m).

We used GEOstationary KOrea Multi-Purpose SATellite 2 A (GEO-KOMPSAT-2 A, GK2A)/Advanced Meteorological Imager (AMI), developed by the National Meteorological Satellite Center (NMSC) of the KMA that was launched on 4 December 2018 (Choi and Ho 2015). GK2A has 16 channels of both visible and infrared wavelengths and provides high temporal-spatial resolution data in 2–10 min over the range of 0.5–2 km. This high quality of data enables us to monitor weather systems more accurately. From GK2A, cloud top temperature (CTT), cloud effective radius (CER), cloud optical thickness (COT), and nighttime cloud optical thickness (NCOT) are used to analyze LTR. The CTT, CER, and COT are known for their utility in detecting precipitable clouds (Ma et al. 2020; Kim et al. 2023a). Also, the CER and COT exhibit positive correlations with rainfall (Ramachandran and Kedia 2013).

CTT is one of the cloud top products derived from the GK2A used to determine the physical characteristics of cloud tops. CTT is defined as the effective temperature at the emission level of the cloud layer radiation. A lower value of CTT implies that clouds are composed of ice particles at higher altitudes. CTT is derived by considering cloud emissivity using optical thickness and radiation correction methods are applied for optically thick clouds (Kim et al. 2019). CTT is retrieved using the visible channel at 8.7 μm and the infrared channel at 10.5, 11.2, 12.3, and 13.3 μm (Choi et al. 2019; Algorithm Theoretical Basis Document (ATBD) in Korean). CTH is calculated using temperature values for each altitude utilizing the temperature profile of the real-time unified model (UM) data. In addition, CTP is a unit conversion of the CTT value using the hydrostatic equation. Since CTH and CTP are derived from CTT, we used CTT as the analysis parameter, which has low uncertainty. CTT enables us to confirm the degree of cloud cooling intuitively.

The relationship between CTT and CER provides insights into the microphysical processes occurring within clouds (Rosenfeld and Lensky 1998). CER is defined as the area-weighted mean radius of cloud droplets, which determines the optical properties of clouds such as reflection, transmission, and absorption (King et al. 1997; Rosenfeld et al. 2012; Ramachandran and Kedia 2013; Kant et al. 2019). The CER represents the radiation characteristics of the cloud as a whole, considering the sizes of the particles in the cloud. CER is retrieved from bi-spectral solar reflectance using visible channels at 0.64 and 0.86 μm, and near-infrared channels at 1.6 μm (Nakajima and King 1990).

COT is a logarithmic value that represents the ratio of attenuation caused by scattering or absorption as light penetrates clouds (Platnick et al. 2016). The COT is based on the vertical profile from the cloud base to the cloud top, using the spectral differences of the brightness temperature between ice and liquid particles (King et al. 1997; Iwabuchi et al. 2016). The visible (VIS) and Short-wave infrared (SWIR) bands utilized for retrieval are appropriate for thick clouds greater than 1 (Nakajima and King 1990). The CER and COT from GK2A are calculated using near-infrared and VIS, respectively (Yang et al. 2019; ATBD in Korean). This method was proposed by Nakajima and King (1990) and was also used by Advanced Baseline Imager (ABI), Moderate Resolution Imaging Spectroradiometer (MODIS), and Spinning Enhanced Visible Infra-Red Imager (SEVIRI) to retrieve CER and COT.

However, CER and COT are available only during the daytime because they are retrieved by visible channels. Therefore, we added NCOT as an alternative variable during the night, which is retrieved similarly to COT using cloud emissivity. NCOT is derived from the infrared channel at 10.5 μm, enabling retrievals even during nighttime periods, when visible channels are unavailable (Minnis and Heck, 2012). Since the background theory of NCOT is more suitable for ice-phase clouds, the reliability of NCOT is generally higher in CC where ice-phase clouds are predominantly distributed.

The uncertainty in CER estimation from optically thick clouds is typically within the range of 1.0–3.0 μm (King et al. 1997). The COT retrieves ice properties with high accuracy between 0.1 and 10. The optimal cloud retrieval rate of CER is greater than 90% when the COT is greater than 1. Uncertain cloud temperatures also cause inaccurate calculation of the CER and COT (Iwabuchi et al. 2016). The CER and COT are only available during the daytime, specifically defined as when the solar zenith angle (SZA) is below 80 degrees. According to Kim et al. (2021), the error of retrieval properties from geostationary satellites increases exponentially in areas with SZA greater than 60 degrees. As a result, retrieval errors exist in the transition zone between day and night. To address the uncertainty in the data, we consider the quality flag of data, pixels with SZA above 66 degrees were excluded.

S-band dual-polarization weather surveillance radar (WSR-88D, RKSG Camp humphreys; 37.21°N, 127.29°W) is used to locate the rain bands and collocate with satellite observations to identify the phase and type of hydrometeors within the clouds (Heiss et al. 1990). The modified hydrometeor classification algorithm in Mahale et al. (2014), which includes three body scattering, is applied. This algorithm utilizes the fuzzy logic method as the operationally used hydrometeor classification algorithm (HCA) from Park et al. (2009). The HCA divides each range gate into the following ten classes: a mixture of rain and hail (RH), heavy rain (HR), light and moderate rain (RA), big drops (BD), graupel (GR), crystals (CR), wet snow (WS), dry aggregated snow (DS), biological scatterers (BS), and ground clutter and anomalous propagation (GC/AP). Polarimetric variables such as the radar reflectivity (Z_H), differential reflectivity, correlation coefficient, and texture parameters of the Z_H and differential phase fields are used to classify the most dominant species in the radar observation. It should be noted that the most dominant species in radar observations do not necessarily agree well with the quantity of cloud microphysical parameters, such as mixing ratio and/or number concentration. For example, the HCA may denote a gate with hail, but the microphysical parameters of hail may not exceed that of rain within the resolution volume. Nevertheless, the classification of hydrometeors in different phases provides insight into the microphysical processes within the cloud.

In addition to classification, radar includes quantitative precipitation estimation and microphysics retrievals of precipitation events (Cao et al. 2010; Mahale et al. 2019; Ryzhkov et al. 2022; Ho et al. 2023). The LWC and D_m are widely used for quantitative analysis and retrievals for data assimilation purposes (Mahale et al. 2019; Ho et al. 2023).

As LWC is directly related to the mixing ratio, and is the 3rd drop size distribution (DSD) moment. In addition, D_m is the ratio of the 4th and 3rd DSD moment and can be used to infer the changes in the raindrop sizes and estimate the DSD in the assumption of exponential DSD. Thus, the physical parameters calculated from polarimetric variables provide physical intuitiveness compared to the six radar variables and are further used for later quantitative analysis. As the exponential DSD model assumption is not valid for very small and large drops, only locations with differential reflectivity (Z_{DR}) values within 0.2 and 4.5 dB were utilized. The equations are as follows:

$$LWC = 0.00050\ Z_h^{\ 0.85}\ Z_{dr}^{\ -3.3} \quad (1)$$

$$D_m = 0.98\ Z_h^{\ 0.046}\ Z_{dr}^{\ 0.91} \quad (2)$$

where the Z_h and Z_{dr} denote the Z_H and differential reflectivity in linear domain ($Z_H = 10\times\log_{10}(Z_h)$ and $Z_{DR} = 10\times\log_{10}(Z_{dr})$, respectively. Note that Eqs. (1) and (2) are only valid for pure rain regimes and were derived based on the DSD in Oklahoma (Ho et al. 2023). However, these assumptions are expected to have limited impact on the analysis results. The pure rain assumption is valid as no hail was reported on the ground during this event. In fact, hail is very rare in Seoul, with no reported hail in August from 1991 to 2020. In addition, the radar used in this study and that used in Oklahoma is the same (i.e., WSR-88D) with identical calibration algorithms. While it is known that the coefficients of the power law relationships depend on the observed DSD, the use of polarimetric variables such as Z_{DR} can account for some of these differences (e.g., Doviak and Zrnic Dúsn 1993). Therefore, the relations in Ho et al. (2023) are adopted for consistency with other algorithms.

The rain rate data was obtained from the Automated Synoptic Observing System (ASOS) data provided by KMA. The observation point of rain rate is Seoul station (WMO number: 47,108, Lon: 127.0°E, Lat: 37.6°E) where the highest rain rate was observed during the research period. The rain rate data was calculated at 10-minute intervals to collocate the time resolution of GK2A.

This study focuses on not the developmental aspects of clouds during their movement, but rather on the observation of precursors when clouds with the potential to induce LTR approach the specified region. Therefore, the concept of monitoring boxes was adopted to observe the changes in values in the local area (Fig. 1). We calculated the temporal variations of GK2A and RKSG cloud products using boxes of 6 km × 6 km, 14 km × 14 km, and 28 km × 28 km (box_6, box_{14}, and box_{28}). Each monitoring box is composed of pixels with a resolution of 2 km. Therefore, box_6, box_{14}, and box_{28} consist of 9, 49, and 196 pixels, respectively. The positions of the monitoring boxes are centered around the

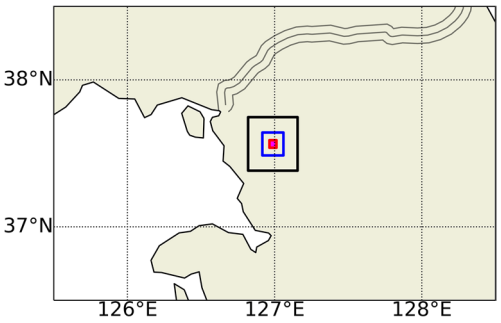


Fig. 1 Illustration of the monitoring boxes. The red box is 6 km × 6 km (box_6), the blue box is 14 km × 14 km (box_{14}), and the black box is 28 km × 28 km (box_{28}). The center of the red box is where Seoul station is located

Seoul station. We excluded clear-sky pixels to consider only cloudy pixels. The box_6 (the red line) is used to focus on a small area. The box_{14} (the blue line) and box_{28} (the black line) are used to monitor middle and large areas, respectively, which follow the criteria based on Geostationary Operational Environmental Satellite Network-12 (GOES-12) (Sieglaff et al. 2011). The box size over 28 km did not yield significant benefits in detecting CC occurring in local areas.

3 Precursory Phenomena before Localized Torrential Rainfall

The cases analyzed in this study correspond to typical LTR events characterized by precipitation durations of less than 24 h and distinct peak rainfall durations within 3 h (Jung et al. 2015). Seoul station recorded several peaks in the intensity of LTR. A cumulative rainfall of 129.6 mm was observed with a maximum rainfall rate of 80.0 mm/h. Among them, three representative LTR periods (P1, P2, and P3) were selected when there was no precipitation in the previous 1 to 2 h, but the precipitation reached its peak in a short time. Although some precipitation peaks existed during P2, the intensity was relatively lower than the others. Therefore, we focus more on the following LTR event.

3.1 P1 (09:30–12:30)

P1 represents the earliest onset of LTR during the study period. Figure 2 shows the time series of cloud properties (CTT, CER, and COT) from GK2A, 3 h before the LTR starts. Note that the radar analysis results are not shown because radar data are not available during this time. While the specific cause of the radar malfunction is unknown, the general radar status message indicated multiple alerts, leading to the radar being placed in maintenance mode. The magenta x marker represents the location of Seoul station. During P1,

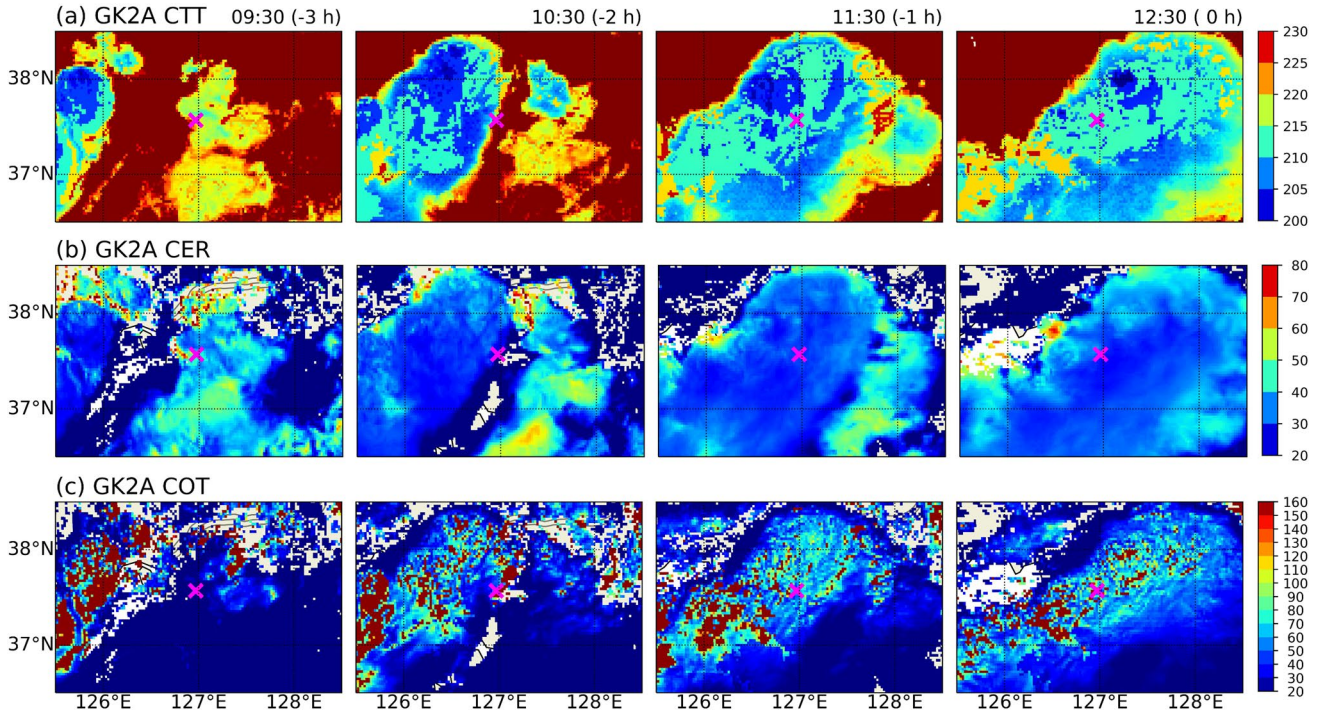


Fig. 2 Time series of cloud properties at 1-hour intervals in P1: (**a**) Cloud top temperature (CTT) [K], (**b**) Cloud effective radius (CER) [μm], and (**c**) Cloud optical thickness (COT) [Unitless]. The 1st column shows 3 h before localized torrential rainfall with the 2nd column (–2 h), 3rd column (–1 h), and 4th column (0 h). The magenta 'x' marker denotes Seoul station

the CTT gradually decreases as the CC approaches Seoul station. In particular, the minimum CTT in CC shows less than 205 K, which indicates that the clouds have already developed enough to produce sufficient precipitation. The CER and COT in CC are distributed inhomogeneously.

Figure 3 represents the changes over time of the minimum CTT, mean CER, and mean COT at Seoul station in P1. When averaging the CTT across all cloudy pixels, the size of cloud region including spread anvil clouds becomes more emphasized than the developing stage of CC. Since this study focuses on the convective core, it is more appropriate to track changes in the minimum value of CTT. In addition, CTT is distributed homogeneously within CC, allowing us to detect the precursor of precipitation using the minimum value within the box. On the other hand, CER and COT are calculated using the mean values within the box since the particles within CC exhibit an inhomogeneous distribution. By considering the mean values, we can reliably identify the precursors of inhomogeneous clouds, as the differences due to box size are not significant. The red, blue, and black dashed lines represent the pixel values of box_6, box_{14}, and box_{28}, respectively. The minimum and mean values of the pixels, excluding clear-sky pixels, are calculated within each box, starting 3 h before the occurrence of LTR at 10-minute intervals. The blue bars represent the observed rain rate at Seoul station.

The CTT decreased steeply 2 h ahead of the onset of LTR and remained low until LTR started (Fig. 3a). All three boxes maintained a low CTT of 210 K. The decreased CTT varies depending on the box size. The CTT decreases by 40, 20, and 10 K for box_6, box_{14}, and box_{28}, respectively. The minimum CTT of box_{28} decreases earlier (from 10:10 to 10:20) than the other boxes (from 10:20 to 10:30). This indicates that box_{28} can detect the precursory phenomena earlier. The increased values in box_6 at 10:10 are attributed to the presence of clouds that are not causing precipitation at that specific moment but are moving through the area. The box_6 is suitable for detecting CC that grows in place and triggers LTR. However, when CC moves and generates precipitation, the performance of LTR detection in box_6 is degraded.

The CER increases from 10:20, which corresponds to the point where the CTT starts to decrease (Fig. 3b). This increase lasts for approximately 20 min. Afterward, CER is maintained up to 30 μm for 2 h. The difference in CER with respect to the box size is not significant. The COT increases sharply, followed by a slight decrease associated with light rainfall around 10:40 and then increases again (Fig. 3c). The COT also increases from box_6 (box_{14}, box_{28}) to more than 45 (40, 30) for 40 min from 10:20, the same time as CER. Similar fluctuations of the values are observed regardless of the box size.

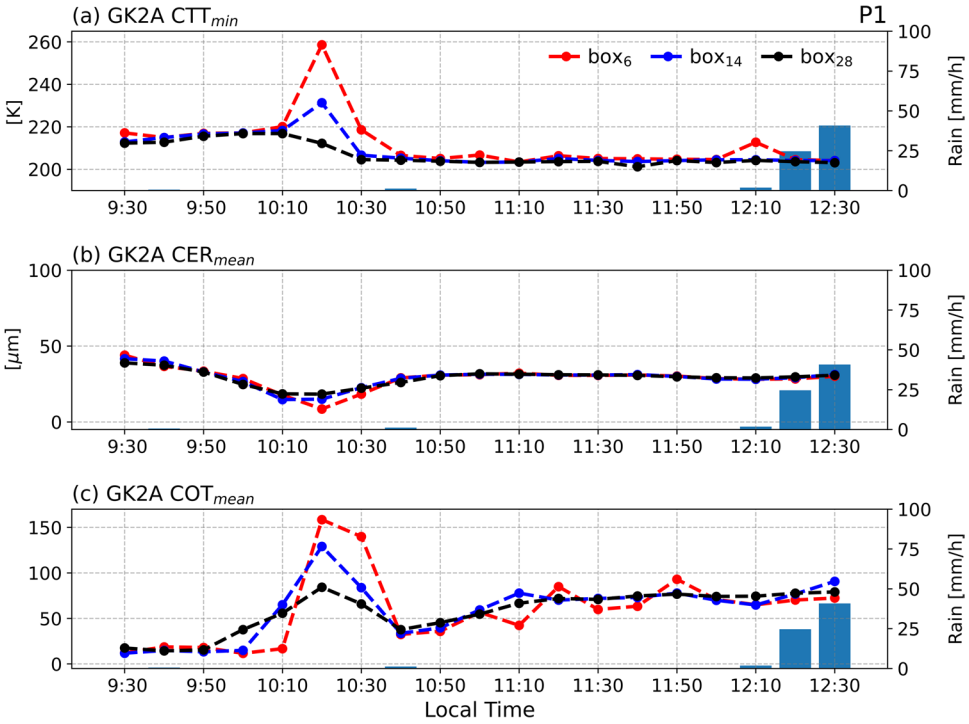


Fig. 3 Time series plots of the cloud properties according to the monitoring box in P1: (**a**) CTT, (**b**) CER, and (**c**) COT. The red, blue, and black dashed lines denote the box$_6$, box$_{14}$, and box$_{28}$, respectively. The blue bar denotes the rain rate [mm/h]

3.2 P2 (14:50–17:50)

P2 shows the highest rain rate among the cases (Fig. 4). Figure 4a–c present the time series of CTT, CER, and COT. Figure 4d–e show Z_H and the HCA vertical cross-section. The x-axis represents the longitude and the y-axis represents the distribution height of the particles. There is no CC observed at 14:50 (–3 h) and observed at the west at − 2 h and moves eastward, getting closer to Seoul station. Convective cells with Z_H up to 50 dBZ start to appear on the western coast with some large drops below 4 km and ice crystals to an altitude of 15 km. From − 2 h, the region below an altitude of 5 km is already covered with rain and large drops in Fig. 4e, probably due to the melting of larger hydrometeors such as graupel and hail.

At 16:50 (–1 h), CC with high Z_H begins and moves northwest of Seoul station. CER and COT are not large within the center of CC, however, COT over 160 at the edges of the CC corresponds with the region of high Z_H (Fig. 4d). As the CC extends from west to east, the continuous supply of optically thick particles might have induced strong LTR. In the lower levels, HCA (Fig. 4e) increases with time with big drops near 126°E as the CC progresses eastward. From 126.5°E to 127.5°E, ice crystals and dry snow are noticed above 16–17 km, which implies strong convection and/or overshooting anvil.

At 17:50 (0 h), the CC is expanded with low CTT and high COT in the vicinity of Seoul station. The strongest radar echo is observed. Heavy rain and/or small hail, along with large drops are noticed around Seoul station. As strong convection continues, ice crystals and dry snow remain up to an altitude of 15 km, and the amount of graupel increases near and above the melting point, which contributes to larger drop sizes below the melting point.

Figure 5 shows the time series of cloud properties in P2. In Fig. 5a, starting one hour before LTR at 16:50, a low CTT of 210 K is observed and maintained. The CTT decreased by 30 K for 20 min in box$_{28}$. The CTT in box$_6$ and box$_{14}$ show a 40 K decrease, which show 10 min later than box$_{28}$. The CER increases over 20 μm for 20 min from 16:30 and then is maintained until LTR occurs (Fig. 5b). Rosenfeld and Gutman (1994) mentioned that CER over 14 μm satisfies the range of precipitable clouds. In addition, areas covered with large COT are more likely to experience precipitation (Chen et al. 2024). In Fig. 5c, the COT increases 40 or more from 16:50 (–1 h) for 30 min (Fig. 5c). In particular, COT in the box$_{28}$ increases more at 17:50 (18 → 78) than at 15:30 (22 → 62), which may generate intense LTR. The LWC is consistently near zero, and a rapid increase just 20 min prior to the LTR (Fig. 5d). LWC exhibits a high value of 1.5 g m^{-3} or more. In box$_{28}$, an increase in values is noticeable around 17:10 (-0.5 h). Note that this rapid increase in LWC allows for the identification of the onset and intensity of precipitation when low CTT remains for over an hour. The increase of D_m occurred relatively slowly compared to LWC, increasing from about 1.1 mm at 17:00 to 1.7 mm at 17:50 (Fig. 5e). Although D_m consistently increased during the period when the CTT was maintained, the rate of change

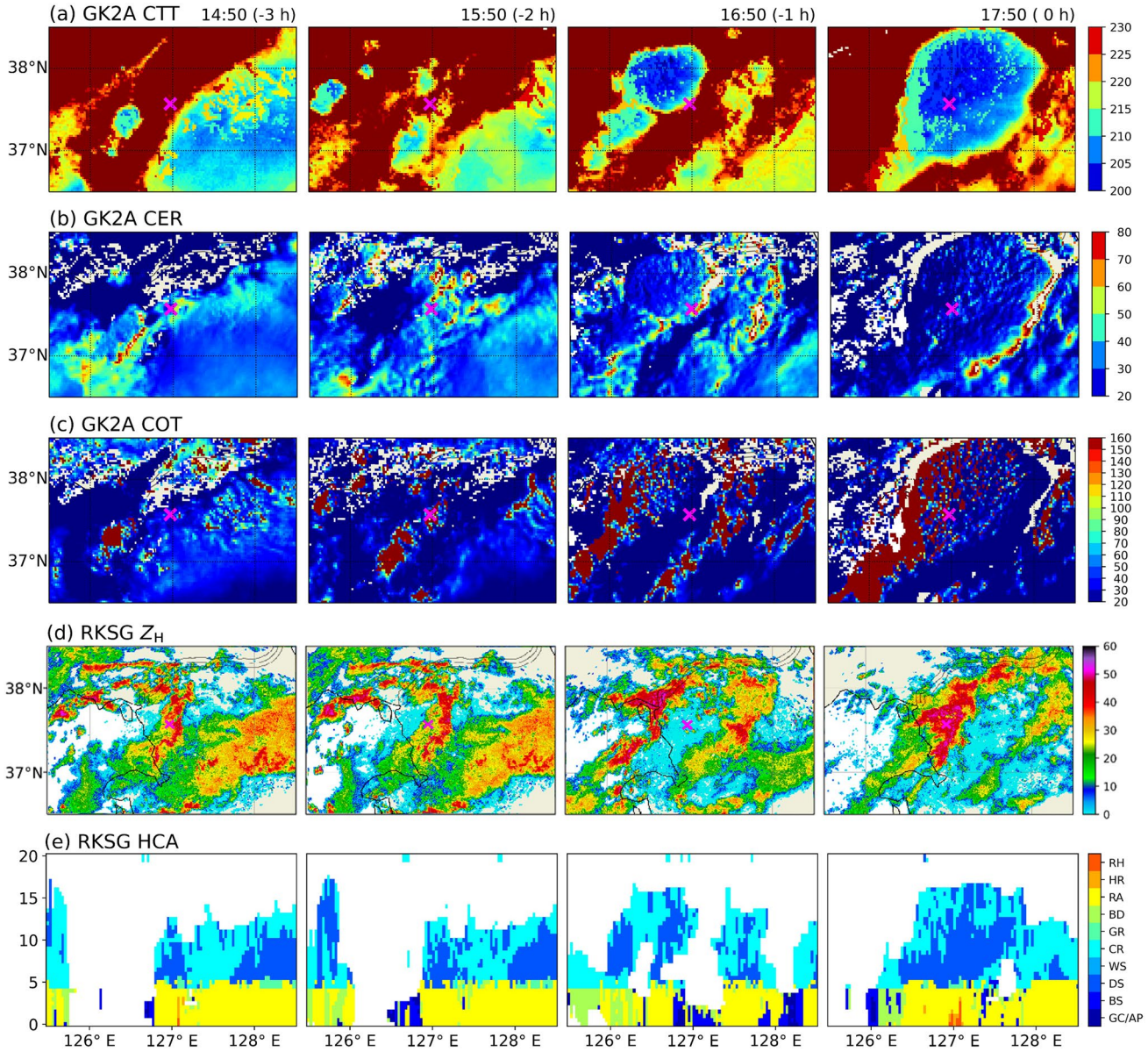


Fig. 4 Time series of cloud properties scene at 1-hour intervals in P2: (**a**) CTT, (**b**) CER, (**c**) COT, (**d**) Radar reflectivity (Z_H) [dBZ], and (**e**) Hydrometeor classification algorithm (HCA). HCA provides a mixture of rain and hail (RH), heavy rain (HR), light and moderate rain (RA), big drops (BD), graupel (GR), crystals (CR), wet snow (WS), dry aggregated snow (DS), biological scatterers (BS), and ground clutter and anomalous propagation (GC/AP)

was much smaller compared to LWC. These results imply that only the number concentration of raindrops increases, and the drop size remains relatively stable even in such a historically significant LTR event with strong convection.

3.3 P3 (18:20–21:20)

After the CC passed that caused LTR in P2, a new CC developed centered on Seoul station, triggering new LTR in P3 (Fig. 6). A new CC is formed at 19:50 (–1.5 h) with a very low CTT and grows rapidly in place. The new CC located very close to Seoul station induces intense LTR. Since CER and COT data are not available at nighttime, NCOT is used instead. The newly formed CC at 20:20 (–1 h) shows large NCOT. High Z_H with a band-shaped pattern implies strong convection and heavy rainfall. Convective cells continually formed along the western coast and progressed into the Seoul metropolitan area. In Fig. 6d, HCA vertically extended up to an altitude of 18 km in a narrow region of clouds composed of ice crystals and dry snow at 127°E, again implying the presence of overshooting anvil due to strong updrafts. Large drops and heavy rain are noticed in the lower levels,

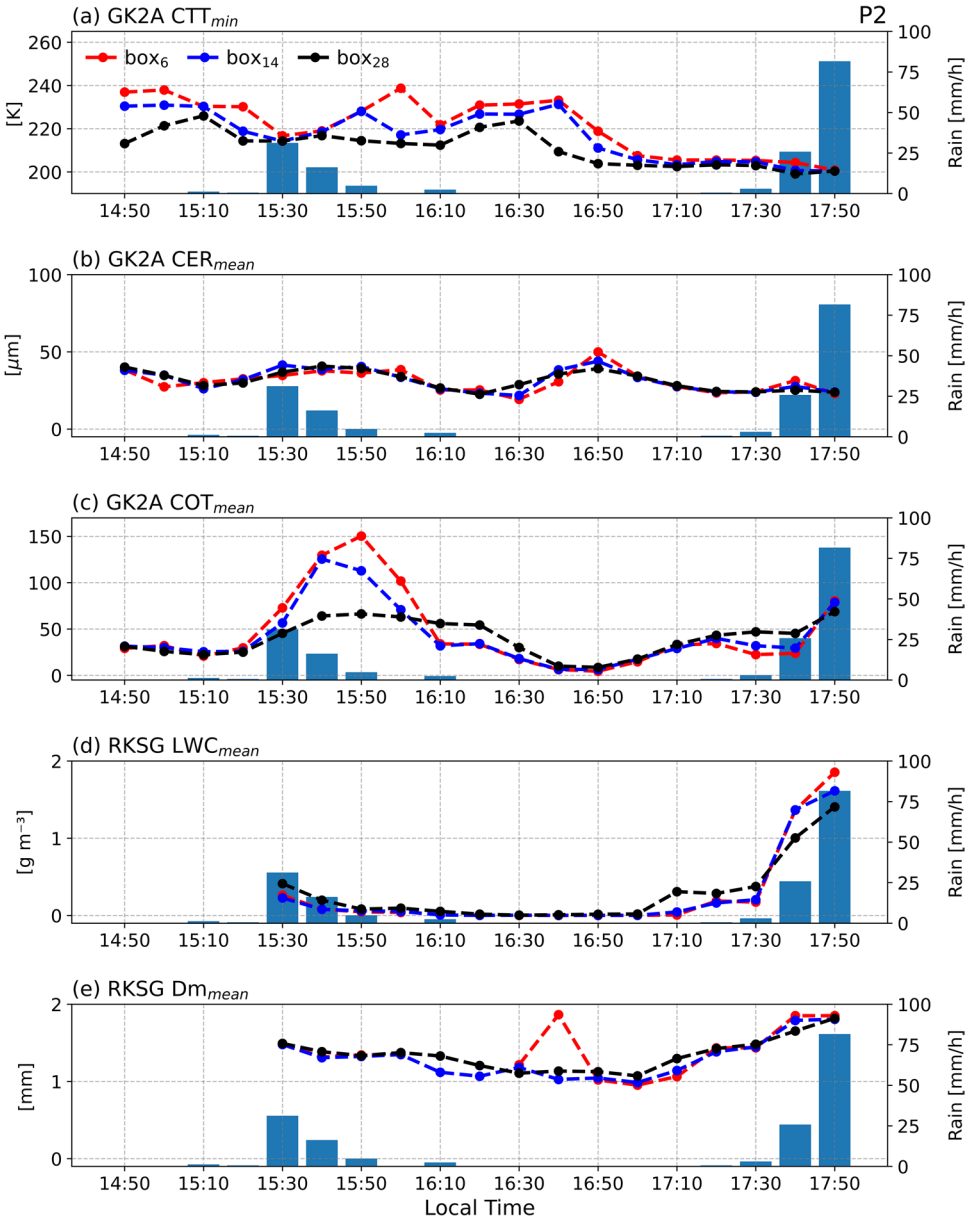


Fig. 5 Time series plots of the cloud properties according to the monitoring box in P2: (**a**) CTT, (**b**) CER, (**c**) COT, (**d**) Liquid water content (LWC) [g m^{-3}], and (**e**) Volume-weighted mean diameter (D_m) [mm]. The red, blue, and black dashed lines denote the box$_6$, box$_{14}$, and box$_{28}$, respectively. The blue bar denotes the rain rate [mm/h]

especially from 125.5°E to 126.5°E where new convection cells continue to form and replace the preexisting cells.

Figure 7 shows the variations of cloud properties in P3. Since the CC of P2 just moved, the CTT starts at a low state of 210 K or less (Fig. 7a). The CTT drops below 10 K for 20 min from 19:30 and has a very low value close to 200 K from 20:20 (–1 h). A minimum CTT of 197 K is observed in box$_{28}$ at 21:10 when the LTR occurs after 10 min. The NCOT decreases when the CC moves in P2 but increases again when a new CC is formed at 20:20 (Fig. 7b). The NCOT increases differently depending on the box size.

P3 is challenging to identify the precursor signals of LTR because convective clouds developed consecutively in place, leading to a sustained low temperature in CTT. However, LWC and D_m show the precursor signals distinctly (Fig. 7c–d). The LWC and D_m increase from 19:30 preceding the rise in NCOT. The box values reached the highest point at the initiation of light rainfall at 20:10. D_m exhibits similar variability to the point where LWC begins to increase.

4 Quantification of LTR Potential as Precursory Signals

We quantitatively calculated the LTR potential (LTR_p) in this section based on Sect. 3. LTR_p [unitless] is defined as the probability of heavy rain. Currently, precipitable water may exist within the cloud due to buoyancy and may not reach the ground (i.e., virga). We referred to Roebeling

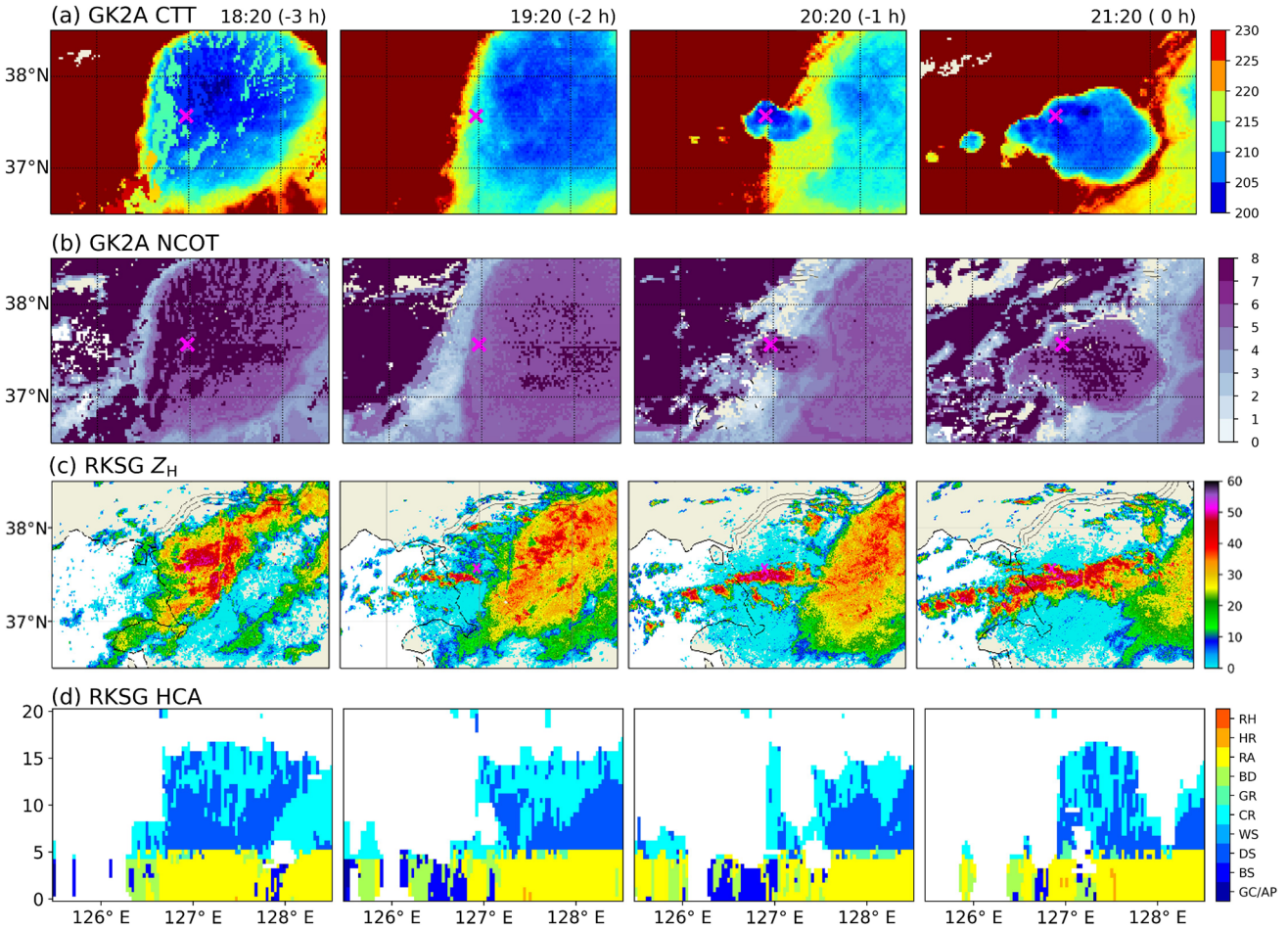


Fig. 6 Time series of cloud properties scene at 1-hour intervals in P3: (**a**) CTT, (**b**) Nighttime cloud optical thickness (NCOT) [Unitless], (**c**) Z_H, and (**d**) HCA

et al. (2012) that proposed an equation for retrieving the R_p using satellite cloud properties (CTT, CER, and COT).

$$\mathrm{CWP} = \frac{2}{3}\,\mathrm{COT}\,\mathrm{CER} \tag{3}$$

where condensed water path (CWP) is calculated by COT and CER in the monitoring box. The CWP provides information for the growth of particles inside the cloud. The $\mathrm{LTR}_{p,\,s}$ is given by

$$\mathrm{LTR}_{p,s} = \frac{c}{H}\left[\frac{\mathrm{CWP} - \mathrm{CWP}_0}{\mathrm{CWP}_0}\right]^{\alpha} \tag{4}$$

where $\mathrm{LTR}_{p,\,s}$ retrieved from GK2A cloud properties only. The CWP is calibrated by CWP_0 and α, which are offset constants 120 g m^{-2} and 1.6. c [mm h^{-1} km] is a constant value of 1. The calibrated CWP is divided by H as follows.

$$H = \frac{\mathrm{CTT}_{max} - \mathrm{CTT}_{min}}{6.5} + \mathrm{dH} \tag{5}$$

where H is the rain column height calculated from the difference between CTT_{max} and CTT_{min} in the monitoring box. Cloud height is divided by a wet adiabatic lapse rate of 6.5 K km^{-1}. The constant dH is set to 0.6 km (Roebeling et al. 2012). The equation and constant are tailored to the Meteosat Second Generation from a European satellite. In addition, radar data was not utilized directly and only referenced to optimize LTR_p (Roebeling and Holleman 2009). This study applied LWC showing a sharp increase before the onset of LTR, to consider LTR_p observed in RKSG. Finally, $\mathrm{LTR}_{p,\,s+r}$ is given by

$$\mathrm{LTR}_{p,s+r} = \frac{c}{H}\left[\frac{\mathrm{CWP} - \mathrm{CWP}_0}{\mathrm{CWP}_0}\right]^{\alpha} + 8\,\mathrm{LWC} \tag{6}$$

Where $\mathrm{LTR}_{p,\,s+r}$ is the LTR_p calculated by a combination of the satellite and radar. We scaled (Scale factor of 8) LTR_p to the rain rate at Seoul station for comparison.

The time series of $\mathrm{LTR}_{p,\,s}$ and $\mathrm{LTR}_{p,\,s+r}$ are shown in Fig. 8. We utilized the box_{28} information that shows

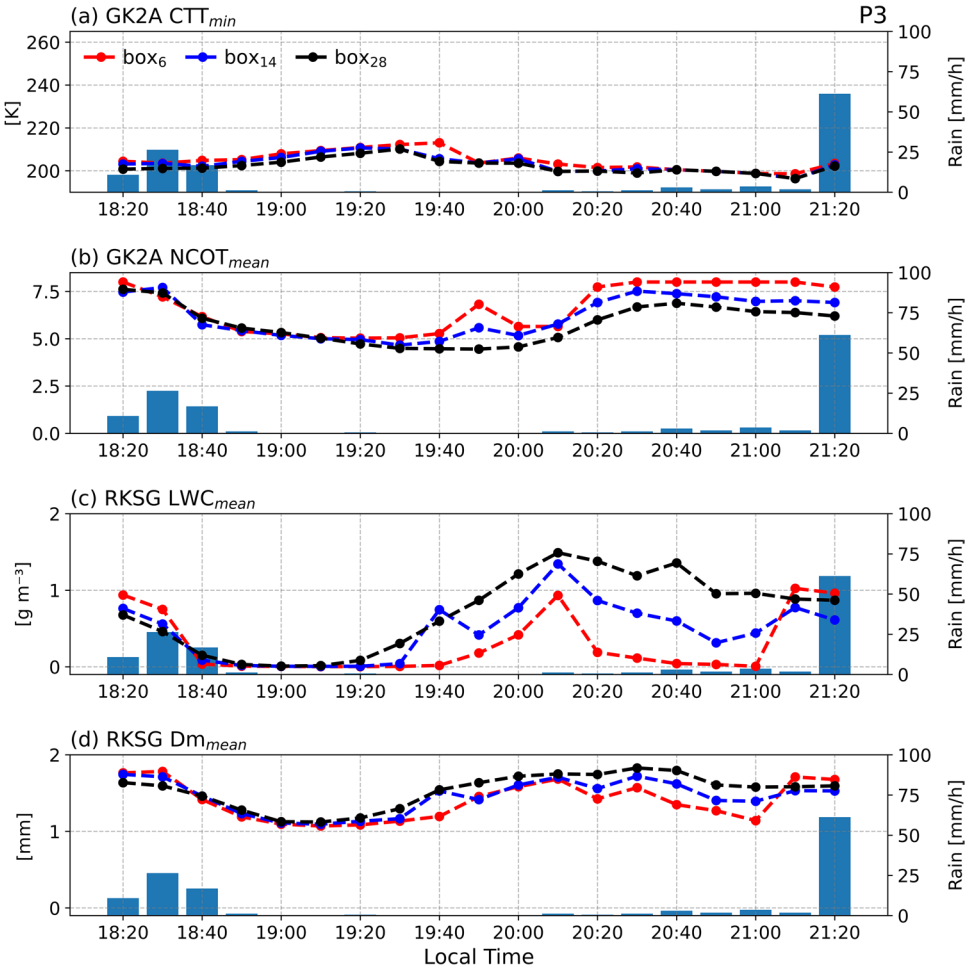


Fig. 7 Time series plots of the cloud properties according to the monitoring box in P3: (**a**) CTT, (**b**) NCOT, (**c**) LWC, and (**d**) D_m

precursory signals of LTR more rapidly than other boxes. The blue bar denotes the measured rain rate from Seoul station. The green line represents $LTR_{p,\,s}$ in Eq. (4) calculated solely using satellite. The $LTR_{p,\,s}$ shows the precursor signals during P1, showing a clear increase starting from 11:00. However, $LTR_{p,\,s}$ does not clearly show the high potential signal at P2. Also, detecting LTR at P3 is difficult where CER and COT cannot be utilized. Moreover, the precursory signal during P3 is difficult to capture by the GK2A because CC is regenerated almost in place. Therefore, radar data is needed to supplement satellite and provide vertical information of CC. The red line represents $LTR_{p,\,s+r}$. RKSG data is provided starting from 15:30 during P2. The inclusion of LWC not only captured rain at P2 effectively, but

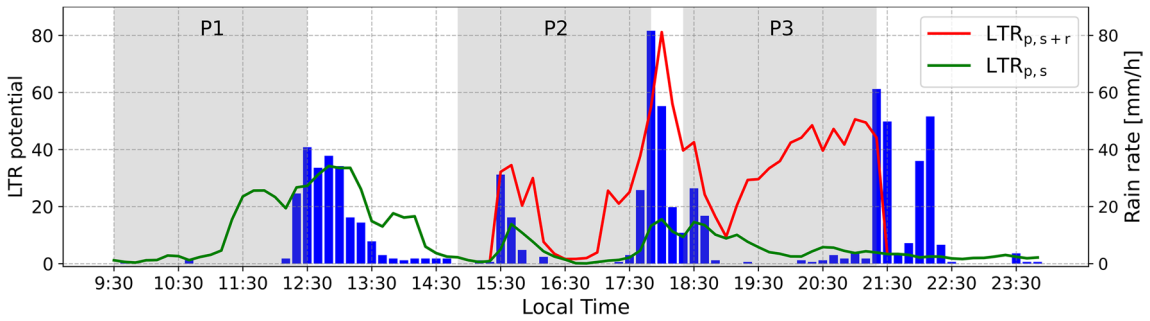


Fig. 8 Time series of LTR potential (LTR_p) [Unitless]. The green and red solid lines denote the LTR potential calculated using satellite ($LTR_{p,\,s}$) and both satellite and radar ($LTR_{p,\,s+r}$), respectively. The blue bar denotes the rain rate [mm/h] measured from Seoul station. The gray shaded areas (P1, P2, and P3) indicate 3 h prior to the occurrence of LTR

also detected increasing precursors from 17:00 and onwards before the onset of LTR. Additionally, even when $LTR_{p,\ s}$ is persistently low in P3 due to the maintenance of low CTT, $LTR_{p,\ s+r}$ shows how potential precursor signals increase before LTR occurs. The precursory signals appeared before LTR started in all cases. In P2 and P3, it is evident that the growth of CC can be identified when combined with radar data. Although the amount of the increase in both $LTR_{p,\ s}$ and $LTR_{p,\ s+r}$, the pattern of increase values before LTR events is consistently observed.

5 Conclusions and Discussions

This study investigated the precursors of LTR events in Korea on August 8, 2022, using remote sensing techniques. We utilized cloud properties (CTT, CER, COT, and NCOT) from remotely sensed cloud properties from GK2A, as well as RKSG observations and their application (Z_H, HCA, LWC, and D_m). In summary, P1 showed the onset of LTR as CC moved from west to east. The CER and COT increased from the point where CTT started to decrease and maintained stable values. P2 represented the highest rain rate among the cases. While the CER and COT showed fluctuations, CTT clearly presented the precursor phenomenon of decreasing and maintaining values. In P3, the strengths of radar become particularly evident. Since the satellite observed only the upper part of the developed clouds, which was challenging to predict the onset of LTR when CC was overlapped. However, the LWC from RKSG clearly increased before LTR occurred. As CCs developed and moved eastward, heavy rain with relatively larger raindrops and/or hail in the lower levels with increased graupel above the melting point was observed. Due to the maintenance of strong convection, large amounts of dry snow and ice crystals extended up to ~ 18 km. We confirmed the variation of cloud physics values before LTR started and calculated LTR_p as the precursory signals of LTR based on satellite and radar. The $LTR_{p,\ s+r}$ showed a better representation of precursor signals and LTR intensity compared to $LTR_{p,\ s}$.

This study highlights that when combining the strengths of these two remote sensing methods, we can overcome the limitations of using either one alone. Geostationary satellites provide valuable information on cloud properties and movement from convective initiation, while radar contributes detailed insights into the internal structure of clouds during precipitation. This dual approach enhances our ability to monitor and forecast severe weather events, providing a more comprehensive and reliable understanding of meteorological phenomena.

Table 1 summarizes the characteristics of cloud properties from both satellite and radar as shown in the present. CTT is a main precursory property of CC among the GK2A cloud properties. In the case of heavy rainfall in the Korean Peninsula, CTT is generally observed to be below 220 K (Park and Park 2020). LTR in this case showed the box value of CTT drops below 220 K, with very strong CCs observed to have CTT < 200 K, and generally maintained a low temperature for 1–1.5 h. These results are consistent with previous studies showing that the CTT of CC reaches its lowest temperature when precipitation peaks, and that prolonged low CTT leads to more intense precipitation (Chen et al. 2024). The CER, COT, and NCOT showed cloud development before LTR but cannot be used independently for pre-detection of LTR due to their high variation. Instead, these variables can be utilized as supplementary variables of CTT to predict LTR events because they increase at the time when CTT drops. In addition, in situations where CER and COT are not available during nighttime, NCOT can be used as an alternative parameter. Although the range of NCOT is smaller (0–8) compared to COT, which ranges from 0 to 160, NCOT still provides sufficient information to identify CC. The radar observations and application supported the properties of CC during LTR. Z_H explicitly showed the movement of rain bands and the location of intense rainfall. In addition, the vertical cross-section of HCA based on the polarimetric radar variables along Seoul station revealed the most dominant hydrometeors before and during LTR. The microphysics parameters (i.e., LWC and D_m) provide

Table 1 Advantages of cloud properties of satellite and radar

Parameter	Advantage
CTT	Precursor confirmation during sustained low temperatures
CER	Supplementary variable to CTT, Detection of cloud development
COT	Supplementary variable to CTT, Detection of cloud development
NCOT	Alternative variables to COT, Applicable during nighttime
Z_H	Locate and quantify precipitation
HCA	Classify multiple types and phases of hydrometers within the convective cloud to infer microphysical processes
LWC	Physically related to mixing ratio, used to retrieve drop size distribution
D_m	Physically related to mixing ratio and number concentration, used to retrieve drop size distribution

microphysical properties, such as drop size distribution of precipitation at the cloud base.

Monitoring boxes around the target point are useful for detecting CC. The box_6 has the advantage of identifying the cells that grow in place. However, the small size of the box is insufficient to capture developing CC as they move. Furthermore, the limited number of pixels can detect significant variability even with minor fluctuations, causing false detection of LTR occurrences. The $box_{28,}$ similar to the box size recommended for cloud detection in Sieglaff et al. (2011), can identify the precursors early, despite the decrease in values being less noticeable. Although our suggested the box size of 28 km is similar to previous findings, further research is needed to determine the most optimal box size for detecting CC. Considering multiple grid information together allows for better predictions. In practical operations for forecasting LTR, grid information at each location can be utilized based on the satellite's resolution of 2 km intervals.

The $LTR_{p,\,s}$ (the LTR potential from satellite data) reveals the precursor signal of LTR but hard to reflect high rainfall intensities. Also, the insufficient data makes LTR detection during nighttime difficult. However, $LTR_{p,\,s+r}$ (the LTR potential from both satellite and radar data) effectively depicts both the precursor of LTR and the peak precipitation. This is attributed to the rapid increase in LWC observed by radar before LTR starts. The findings from this study imply that investigating more LTR events is needed to improve nowcasting for LTR occurrences in the future. Especially, the research is needed to optimize the equation suggested in this study for the Korean Peninsula to improve LTR nowcasting. We presume that the present methods may be appropriate for the rapidly developing or back-building formation of CCs, not for continuous rainfall caused by typhoons or frontal systems.

The estimation of LTR potential using a combination of geostationary satellite and radar remote sensing data can effectively monitor the precursors of LTR. This study suggests that using both instruments can provide high-resolution forecasts in real-time and allow for adequate preparedness. Further studies should focus on identifying the characteristics of CC more precisely before LTR starts, which will help advance prediction for heavy rainfall.

Acknowledgements This research was supported by Basic Science Research Program through the National Research Foundation of Korea (NRF) funded by the Ministry of Education (2018R1A6A1A08025520) and the National Research Foundation of Korea (NRF) grant funded by the Korea government (MSIT) (2021R1A2C1093402).

Declarations

Conflict of Interest The authors have no conflicts of interest to declare.

Open Access This article is licensed under a Creative Commons Attribution 4.0 International License, which permits use, sharing, adaptation, distribution and reproduction in any medium or format, as long as you give appropriate credit to the original author(s) and the source, provide a link to the Creative Commons licence, and indicate if changes were made. The images or other third party material in this article are included in the article's Creative Commons licence, unless indicated otherwise in a credit line to the material. If material is not included in the article's Creative Commons licence and your intended use is not permitted by statutory regulation or exceeds the permitted use, you will need to obtain permission directly from the copyright holder. To view a copy of this licence, visit http://creativecommons.org/licenses/by/4.0/.

References

Bluestein, H.B., Jain, M.H.: Formation of mesoscale lines of precipitation: severe squall lines in Oklahoma during the spring. J. Atmos. Sci. **42**(16), 1711–1732 (1985). https://doi.org/10.1175/1520-0469(1985)042<1711:FOMLOP>2.0.CO;2

Cao, Q., Zhang, G., Brandes, E.A., Schuur, T.J.: Polarimetric radar rain estimation through retrieval of drop size distribution using a bayesian approach. J. Appl. Meteorol. Climatol. **49**(5), 973–990 (2010). https://doi.org/10.1175/2009JAMC2227.1

Chappell, C.F.: Quasi-stationary convective events. In: Mesoscale Meteorology and Forecasting, pp. 289–310. Springer (1986). https://doi.org/10.1007/978-1-935704-20-1_13

Chen, X., Letu, H., Shang, H., Ri, X., Tang, C., Ji, D., Shi, C., Teng, Y.: Rainfall Area Identification Algorithm Based on Himawari-8 Satellite Data and Analysis of its Spatiotemporal Characteristics. Remote Sensing, **16**(5), 747 (2024). https://doi.org/10.3390/rs16050747

Choi, Y.-S., Ho, C.-H.: Earth and environmental remote sensing community in South Korea: A review. Remote Sens. Appl.: Soc. Environ. **2**, 66–76 (2015). https://doi.org/10.1016/j.rsase.2015.11.003

Choi, Y.-S., Kim, H.-S., Kwon, M.-J.: GK-2A AMI Algorithm Theoretical Basis Document (ATBD) Cloud Top Products. National Meteorological Satellite Center (NMSC), Jincheon, Korea (2019)

Doviak, R.J., Zrníc Dúsn, S.: Doppler Radar and Weather Observations. Academic, San Diego, CA (1993)

Ellis, S.M., Vivekanandan, J.: Liquid water content estimates using simultaneous S and k a band radar measurements. Radio. Sci. **46**(02), 1–15 (2011). https://doi.org/10.1029/2010RS004361

Haberlie, A. M., Ashley, W. S.: A radar-based climatology of mesoscale convective systems in the United States. J. Climate. **32**(5), 1591-1606 (2019). https://doi.org/10.1175/JCLI-D-18-0559.13

Ha, J.-H., Kim, H.-W., Lee, D.-K.: Observation and numerical simulations with radar and surface data assimilation for heavy rainfall over central Korea. Adv. Atmos. Sci. **28**, 573–590 (2011). https://doi.org/10.1007/s00376-010-0035-y

Heiss, W.H., McGrew, D.L., Sirmans, D.: NEXRAD: Next generation weather radar (WSR-88D). Microw. J. **33**(1), 79–89 (1990)

Hitchcock, S.M., Schumacher, R.S.: Analysis of back-building convection in simulations with a strong low-level stable layer. Mon. Weather Rev. **148**(9), 3773–3797 (2020). https://doi.org/10.1175/MWR-D-19-0246.1

Ho, J., Zhang, G., Bukovcic, P., Parsons, D.B., Xu, F., Gao, J., Carlin, J.T., Snyder, J.C.: Improving Polarimetric Radar-based Drop size distribution Retrieval and rain estimation using a deep neural network. J. Hydrometeorol. **24**(11), 2057–2073 (2023). https://doi.org/10.1175/JHM-D-22-0166.1

Hong, S.-Y., Kwon, Y.C., Kim, T.-H., Kim, E., Choi, J.-E., Kwon, S.-J., Kim, I.-H., Lee, J., Park, E.-H., Kim, D.-I.: The Korean Integrated Model (KIM) system for global weather forecasting. Asia-Pac. J. Atmos. Sci. **54**, 267–292 (2018). https://doi.org/10.1007/s13143-018-0028-9

Ivanova, A.: International practices of thunderstorm nowcasting. Russ. Meteorol. Hydrol. **44**, 756–763 (2019). https://doi.org/10.3103/S1068373919110050

Iwabuchi, H., Saito, M., Tokoro, Y., Putri, N.S., Sekiguchi, M.: Retrieval of radiative and microphysical properties of clouds from multispectral infrared measurements. Progress Earth Planet. Sci. **3**, 1–18 (2016). https://doi.org/10.1186/s40645-016-0108-3

Jeong, J.-H., Lee, D.-I., Wang, C.-C.: Impact of the cold pool on mesoscale convective system–produced extreme rainfall over southeastern South Korea: 7 July 2009. Mon. Weather Rev. **144**(10), 3985–4006 (2016). https://doi.org/10.1175/MWR-D-16-0131.1

Jones, W.K., Christensen, M.W., Stier, P.: A semi-lagrangian method for detecting and tracking deep convective clouds in geostationary satellite observations. Atmos. Meas. Tech. **16**(4), 1043–1059 (2023). https://doi.org/10.5194/amt-16-1043-2023

Jung, I.W., Bae, D.H., Kim, G.: Recent trends of mean and extreme precipitation in Korea. Int. J. Climatol. **31**(3), 359–370 (2011). https://doi.org/10.1002/joc.2068

Jung, S.-P., Kwon, T.-Y., Han, S.-O., Jeong, J.-H., Shim, J., Choi, B.-C.: Thermodynamic characteristics associated with localized torrential rainfall events in the southwest region of the Korean peninsula. Asia-Pac. J. Atmos. Sci. **51**, 229–237 (2015). https://doi.org/10.1007/s13143-015-0073-6

Kant, S., Panda, J., Pani, S.K., Wang, P.K.: Long-term study of aerosol–cloud–precipitation interaction over the eastern part of India using satellite observations during pre-monsoon season. Theoret. Appl. Climatol. **136**, 605–626 (2019). https://doi.org/10.1007/s00704-018-2509-2

Kim, H.-S., Baum, B.A., Choi, Y.-S.: Use of spectral cloud emissivities and their related uncertainties to infer ice cloud boundaries: Methodology and assessment using CALIPSO cloud products. Atmos. Meas. Tech. **12**(9), 5039–5054 (2019). https://doi.org/10.5194/amt-12-5039-2019

Kim, G., Choi, Y.-S., Park, S.S., Kim, J.: Effect of solar zenith angle on satellite cloud retrievals based on O2–O2 absorption band. Int. J. Remote Sens. **42**(11), 4224–4240 (2021). https://doi.org/10.1080/01431161.2021.1890267

Kim, D., Kim, H.-J., Choi, Y.-S.: Unsupervised clustering of Geostationary Satellite Cloud properties for estimating precipitation probabilities of Tropical Convective clouds. J. Appl. Meteorol. Climatol. **62**(8), 1083–1094 (2023a). https://doi.org/10.1175/JAMC-D-22-0175.1

Kim, H.-A., Ho, J., Zhang, G., Ha, K.-J., Hong, S.-Y., Ho, C.-H.: Polarimetric Radar Signatures in various lightning activities during Seoul (Korea) Flood on August 8, 2022. Asia-Pac. J. Atmos. Sci. 1–15 (2023b). https://doi.org/10.1007/s13143-023-00346-0

King, M.D., Tsay, S.-C., Platnick, S.E., Wang, M., Liou, K.-N.: Cloud retrieval algorithms for MODIS: Optical thickness, effective particle radius, and thermodynamic phase. MODIS Algorithm Theoretical Basis Document, **1997**, 440 (1997)

Lee, T.-Y., Kim, Y.-H.: Heavy precipitation systems over the Korean peninsula and their classification. Asia-Pac. J. Atmos. Sci. **43**(4), 367–396 (2007)

Lee, H., Baik, J.J.: Effects of turbulence-induced collision enhancement on heavy precipitation: The 21 September 2010 case over the Korean Peninsula. J. Geophys. Res. Atmos **121**(20), 12,319-312,342 (2016). https://doi.org/10.1002/2016JD025168

Lee, H., Baik, J.-J.: A comparative study of bin and bulk cloud microphysics schemes in simulating a heavy precipitation case. Atmosphere **9**(12), 475 (2018). https://doi.org/10.3390/atmos9120475

Ma, Z., Xu, J., He, K., Han, X., Ji, Q., Wang, T., Xiong, W., Hong, Y.: An updated moving window algorithm for hourly-scale satellite precipitation downscaling: A case study in the Southeast Coast of China. J. Hydrol. **581**, 124378 (2020). https://doi.org/10.1016/j.jhydrol.2019.124378

Mahale, V.N., Zhang, G., Xue, M.: Fuzzy logic classification of S-band polarimetric radar echoes to identify three-body scattering and improve data quality. J. Appl. Meteorol. Climatology **53**(8), 2017–2033 (2014). https://doi.org/10.1175/JAMC-D-13-0358.1

Mahale, V.N., Zhang, G., Xue, M., Gao, J., Reeves, H.D.: Variational retrieval of rain microphysics and related parameters from polarimetric radar data with a parameterized operator. J. Atmos. Ocean. Technol. **36**(12), 2483–2500 (2019). https://doi.org/10.1175/JTECH-D-18-0212.1

Minnis, P., Heck, P.W.: GOES-R Advanced Baseline Imager (ABI) Algorithm Theoretical Basis Document for Nighttime Cloud Optical Depth, Cloud Particle Size, Cloud Ice Water Path, and Cloud Liquid Water Path. NOAA/NESDIS Center for Satellite Applications and Research; 2012. Available online: https://www.star.nesdis.noaa.gov/goesr/documents/ATBDs/Baseline/ATBD_GOESR_Cloud_NCOMP_v3.0_Jul2012.pdf. Accessed 10 July 2024

Müller, R., Barleben, A., Haussler, S., Jerg, M.: A Novel Approach for the Global Detection and nowcasting of deep convection and thunderstorms. Remote Sens. **14**(14), 3372 (2022). https://doi.org/10.3390/rs14143372

Nakajima, T., King, M.D.: Determination of the optical thickness and effective particle radius of clouds from reflected solar radiation measurements. Part I: Theory. J. Atmos. Sci. **47**(15), 1878–1893 (1990). https://doi.org/10.1175/1520-469(1990)047<1878:DOTOTA>2.0.CO;2

Okazaki, A., Honda, T., Kotsuki, S., Yamaji, M., Kubota, T., Oki, R., Iguchi, T., Miyoshi, T.: Simulating precipitation radar observations from a geostationary satellite. Atmospheric Measurement Techniques **12**(7), 3985–3996 (2019). https://doi.org/10.5194/amt-12-3985-2019

Park, S.K., Park, S.: On a flood-producing coastal mesoscale convective storm associated with the Kor'easterlies: Multi-data analyses using remotely-sensed and in-situ observations and storm-scale model simulations. Remote Sens. **12**(9), 1532 (2020). https://doi.org/10.3390/rs12091532

Park, H.S., Ryzhkov, A.V., Zrnić, D., Kim, K.-E.: The hydrometeor classification algorithm for the polarimetric WSR-88D: Description and application to an MCS. Weather Forecast. **24**(3), 730–748 (2009). https://doi.org/10.1175/2008WAF2222205.1

Platnick, S., Meyer, K.G., King, M.D., Wind, G., Amarasinghe, N., Marchant, B., Arnold, G.T., Zhang, Z., Hubanks, P.A., Holz, R.E.: The MODIS cloud optical and microphysical products: Collection 6 updates and examples from Terra and Aqua. IEEE Trans. Geosci. Remote Sens. **55**(1), 502–525 (2016). https://doi.org/10.1109/TGRS.2016.2610522

Ramachandran, S., Kedia, S.: Aerosol, clouds and rainfall: Inter-annual and regional variations over India. Clim. Dyn. **40**, 1591–1610 (2013). https://doi.org/10.1007/s00382-012-1594-7

Roebeling, R., Holleman, I.: SEVIRI rainfall retrieval and validation using weather radar observations. J. Geophys. Research: Atmos. **114**(D21) (2009). https://doi.org/10.1029/2009JD012102

Roebeling, R., Wolters, E., Meirink, J., Leijnse, H.: Triple collocation of summer precipitation retrievals from SEVIRI over Europe with gridded rain gauge and weather radar data. J. Hydrometeorol. **13**(5), 1552–1566 (2012). https://doi.org/10.1175/JHM-D-11-089.1

Rosenfeld, D., Gutman, G.: Retrieving microphysical properties near the tops of potential rain clouds by multispectral analysis of AVHRR data. Atmos. Res. **34**(1–4), 259–283 (1994). https://doi.org/10.1016/0169-8095(94)90096-5

Rosenfeld, D., Lensky, I.M.: Satellite-based insights into precipitation formation processes in continental and maritime convective clouds. Bull. Am. Meteorol. Soc. **79**(11), 2457–2476 (1998). https://doi.org/10.1175/1520-0477(1998)079<2457:SBIIPF>2.0.CO;2

Rosenfeld, D., Wang, H., Rasch, P.J.: The roles of cloud drop effective radius and LWP in determining rain properties in marine stratocumulus. Geophys. Res. Lett. **39**(13) (2012). https://doi.org/10.1029/2012GL052028

Ryzhkov, A., Zhang, P., Bukovčić, P., Zhang, J., Cocks, S.: Polarimetric radar quantitative precipitation estimation. Remote Sens. **14**(7), 1695 (2022). https://doi.org/10.3390/rs14071695

Schumacher, R.S.: Heavy rainfall and flash flooding. In Oxford research encyclopedia of natural hazard science. (2017). https://doi.org/10.1093/acrefore/9780199389407.013.132

Schumacher, R.S., Johnson, R.H.: Organization and environmental properties of extreme-rain-producing mesoscale convective systems. Mon. Weather Rev. **133**(4), 961–976 (2005). https://doi.org/10.1175/MWR2899.1

Shin, U., Park, S.-H., Yun, Y.-R., Oh, C.: Synoptic features of August Heavy Rainfall episodes Accompanied by a Quasi-stationary Front over the Korean Peninsula and its relationship with the Western Pacific Subtropical High. Front. Earth Sci. **10**, 940785 (2022). https://doi.org/10.3389/feart.2022.940785

Sieglaff, J.M., Cronce, L.M., Feltz, W.F., Bedka, K.M., Pavolonis, M.J., Heidinger, A.K.: Nowcasting convective storm initiation using satellite-based box-averaged cloud-top cooling and cloud-type trends. J. Appl. Meteorol. Climatology **50**(1), 110–126 (2011). https://doi.org/10.1175/2010JAMC2496.1

Yang, Y., Yum, S.S., Um, J.: GK-2A AMI Algorithm Theoretical Basis Document (ATBD) Daytime Cloud Optical Thickness and Cloud Microphysics Retrieval Algorithm. National Meteorological Satellite Center (NMSC), Jincheon, Korea (2019)

You, C., Kang, M., Lee, D.-I.: Rainfall estimates with respect to rainfall types using S-band polarimetric radar in Korea. Atmosphere **10**(12), 773 (2019). https://doi.org/10.3390/atmos10120773

Publisher's Note Springer Nature remains neutral with regard to jurisdictional claims in published maps and institutional affiliations.